

# Soft Matter

Accepted Manuscript

This article can be cited before page numbers have been issued, to do this please use: M. B. Khan, A. Patterson, J. Ali, T. Siegrist, M. Humayun and H. Mohammadigoushki, *Soft Matter*, 2026, DOI: 10.1039/D6SM00260A.



This is an Accepted Manuscript, which has been through the Royal Society of Chemistry peer review process and has been accepted for publication.

Accepted Manuscripts are published online shortly after acceptance, before technical editing, formatting and proof reading. Using this free service, authors can make their results available to the community, in citable form, before we publish the edited article. We will replace this Accepted Manuscript with the edited and formatted Advance Article as soon as it is available.

You can find more information about Accepted Manuscripts in the [Information for Authors](#).

Please note that technical editing may introduce minor changes to the text and/or graphics, which may alter content. The journal's standard [Terms & Conditions](#) and the [Ethical guidelines](#) still apply. In no event shall the Royal Society of Chemistry be held responsible for any errors or omissions in this Accepted Manuscript or any consequences arising from the use of any information it contains.

Cite this: DOI: 00.0000/xxxxxxxxxx

# Dynamics of Weakly Magnetic Nanoparticle Suspensions Near a Magnetized Sphere

Mohd Bilal Khan<sup>a,b</sup>, Abigail Patterson<sup>a,b</sup>, Jamel Ali<sup>a,b</sup>, Theo Siegrist<sup>a,b</sup>, Munir Humayun<sup>a,c</sup>, Hadi Mohammadigoushki<sup>a,b</sup>

Received Date  
Accepted Date

DOI: 00.0000/xxxxxxxxxx

We report experimental and multiphysics simulation studies of magnetophoretic transport and capture of nanoparticles around a magnetized sphere under high-gradient magnetic fields. Experiments were performed using a broad range of paramagnetic and diamagnetic nanoparticles at an imposed magnetic field up to  $\mathbf{B}_0 = 1$  T and concentrations of  $c_0 = 10\text{--}100$  mg/L. Paramagnetic nanoparticles exhibited substantially enhanced capture compared to diamagnetic nanoparticles, with capture efficiency increasing nonlinearly with magnetic field strength, initial nanoparticle concentration, and magnetic susceptibility. In addition, increasing sphere diameter also improved capture efficiency of paramagnetic nanoparticles despite reducing local magnetic field gradients. Our analysis showed that the observed rate of nanoparticles capture by the non-uniform magnetic-field exceeded predictions from a simple scaling analysis and isolated-particle magnetophoresis. More detailed analysis using multiphysics numerical simulations suggest magnetic field-induced nanoparticle clustering, which in turn significantly enhances transport of nanoparticles. In addition, field-induced convective flows were found to substantially promote nanoparticle transport. These results highlight that magnetophoretic capture of weakly paramagnetic materials in high-gradient magnetic systems is governed by a nonlinear coupling of magnetic and flow-driven transport mechanisms. These results provide insights into the design of magnetic separation systems for recovery and recycling weakly magnetic nanoparticles and colloidal suspensions.

## 1 Introduction

The selective capture of nanoparticles in suspension underpins a broad range of technologies, including water treatment<sup>1</sup>, mineral processing<sup>2</sup>, biomedical imaging<sup>3</sup>, resource recovery<sup>4</sup>, and targeted therapies<sup>5</sup>. In particular, the recovery of critical metals from end-of-life electronics, batteries, and permanent magnets, as well as the purification of industrial effluents, increasingly requires the separation of weakly paramagnetic and diamagnetic nanoparticles<sup>6–11</sup>. Conventional separation methods such as filtration, centrifugation, and sedimentation are often ineffective at the nanoscale due to the particles' negligible inertia, strong Brownian agitation, and potential chemical or environmental hazards<sup>12–15</sup>. Magnetically assisted separation has therefore emerged as a non-invasive and energy-efficient alternative for isolating weakly magnetic nanoparticles<sup>16,17</sup>. Magnetophoresis, the underlying physical principle for magnetically as-

sisted separation, exploits differences in magnetic susceptibility in the presence of strong magnetic-field gradients. Nanoparticles with positive magnetic susceptibility (paramagnetic) are drawn toward regions of high field intensity. In contrast, particles with negative susceptibility (diamagnetic) experience a repulsive force and thus exhibit little or no retention under comparable conditions<sup>18</sup>

The study of magnetophoresis spans more than five decades and encompasses a broad spectrum of particle types, magnetic field strengths, and separation architectures<sup>18</sup>. Two distinct regimes dominate the literature, high-gradient magnetic separation (HGMS), which employs ferromagnetic matrices that generate extremely strong local field to capture strongly magnetic particles, and low-gradient magnetic separation (LGMS), which exploits weaker fields yet can yield unexpectedly rapid removal of superparamagnetic nanoparticles<sup>19</sup>. Classical HGMS focuses on micron- and nanometer-scale particles with relatively large magnetic susceptibilities<sup>20–26</sup>. In contrast, LGMS typically operates with much weaker gradients yet has been shown to remove superparamagnetic nanoparticles at rates far exceeding those predicted by single-particle magnetophoretic theory<sup>19,27–31</sup>. Early experimental work revealed removal efficiencies far higher than

<sup>a</sup> Department of Chemical and Biomedical Engineering, Florida State University, Tallahassee, Florida, United States-32310.; E-mail: hadi.moham@eng.famu.fsu.edu

<sup>b</sup> Center for Rare Earths, Critical Minerals, and Industrial Byproducts, National High Magnetic Field Laboratory, Tallahassee, FL 32310, USA

<sup>c</sup> Department of Earth, Ocean and Atmospheric Science, Florida State University, Tallahassee, FL 32304, USA.



40 expected for isolated nano-particles migrating through quiescent 96  
41 fluids<sup>19</sup>. This discrepancy led to the hypothesis that applied 97  
42 magnetic fields induce reversible nanoparticle clustering, which 98  
43 may in turn create larger, and more magnetically responsive ag- 99  
44 gregates that experience substantially greater magnetophoretic 100  
45 forces<sup>32–39</sup>. 101

46 Despite significant advances in both HGMS and LGMS, par-102  
47 ticularly for superparamagnetic iron-oxide nanoparticles and mi-103  
48 croparticles, a substantial gap remains in understanding magne-104  
49 tophoresis of weakly paramagnetic and diamagnetic nanoparti-105  
50 cles that are relevant to the critical materials found in electronic  
51 waste (e.g., Nickel, Cobalt, Manganese, Bismuth, Zinc, among<sup>106</sup>  
52 others). As the volume of spent electronic waste continues to 107  
53 grow, recovering, and reusing these critical metals has become 108  
54 increasingly important for reducing dependence on natural re-109  
55 sources, strengthening supply chains, and mitigating environ-110  
56 mental impacts<sup>40,41</sup>. These species have magnetic susceptibil-111  
57 ities orders of magnitude smaller than those of superparamag-  
58 netic systems, placing them in a regime where magnetophoretic  
59 transport competes strongly with Brownian diffusion<sup>29</sup>. Recent  
60 work indicates that, beyond field-induced clustering observed in  
61 super paramagnetic nanoparticle suspensions, weakly magnetic  
62 nanoparticles may also experience field-driven convective flows  
63 that enhance their transport and separation<sup>42,43</sup>. Furthermore,  
64 the field-induced convective flows could be substantially ampli-  
65 fied in the vicinity of magnetized ferromagnetic wires<sup>43</sup>.

66 Although spherical ferromagnetic collectors have been shown  
67 to efficiently capture superparamagnetic nanoparticles<sup>44–46</sup>, the  
68 magnetophoretic transport of weakly magnetic nanoparticles  
69 near a magnetized sphere remains comparatively underexplored. 112  
70 Most prior studies have focused on superparamagnetic parti- 113  
71 cles, whose large magnetic susceptibilities produce strong magne- 114  
72 tophoretic forces and rapid capture. In contrast, weakly paramag- 115  
73 netic and diamagnetic nanoparticles require substantially higher  
74 magnetic field gradients for effective manipulation. Moreover, 116  
75 the coupled effects of nanoparticle magnetic susceptibility, initial  
76 concentration, and applied magnetic field strength on capture ef- 117  
77 ficiency of weakly paramagnetic and diamagnetic particles have  
78 not been systematically investigated. The roles of field-induced  
79 particle clustering, and magneticay driven convective flows near 120  
80 magnetized ferromagnetic collectors also remain poorly under- 121  
81 stood, which makes it unclear whether such mechanisms estab- 122  
82 lished for superparamagnetic particles can be leveraged for the 123  
83 separation of weakly paramagnetic or diamagnetic nanoparticles. 124  
84 In summary, the transport behavior of weakly magnetic nanopar- 125  
85 ticles in localized high-gradient magnetic fields remains poorly 126  
86 understood, and a coupled experimental and multiphysics nu- 127  
87 merical simulations is needed to enable a more in-depth under- 128  
88 standing of the mechanisms involved in magnetophoresis of these 129  
89 systems. 130

90 The main goal of this study is to provide an in-depth analy-  
91 sis of magnetophoretic motion of weakly paramagnetic and dia-131  
92 magnetic nanoparticles under a high gradient magnetic field. To 132  
93 accomplish this goal, we will investigate the magnetophoresis dy-133  
94 namics of a diverse set of weakly paramagnetic ( $\text{Mn}_2\text{O}_3$ ,  $\text{Co}_2\text{O}_3$ ,<sup>134</sup>  
95  $\text{Fe}_2\text{O}_3$ ,  $\text{CuO}$ ) and diamagnetic ( $\text{Bi}_2\text{O}_3$ ,  $\text{ZnO}$ ) nanoparticles in the<sup>135</sup>

vicinity of a magnetized stainless-steel sphere. These metal oxides  
are commonly found in spent batteries and other electronic waste  
components such as cathode/anode materials, protective casings,  
and PCBs<sup>47,48</sup>. We will perform systematic experiments over a  
broad range of initial concentrations, imposed magnetic field,  
and magnetic susceptibility. The experimental measurements are  
complemented by three-dimensional multiphysics numerical sim-  
ulations, which in turn enable detailed analysis of field-induced  
cluster formation, field-driven convective flows, and flow struc-  
tures around the magnetized sphere.

## 2 Experiments

### 2.1 Materials

Paramagnetic and diamagnetic nano-particles with various mag-  
netic susceptibilities were obtained from Sigma-Aldrich and used  
as received. Their magnetic susceptibility values and vendor pro-  
vided sizes are presented in Table (1).

Table 1 A summary of nano-particles used in this study along with their  
most relevant properties. \*Specified by vendor. Here  $\Delta\chi_v = \chi_v|_{\text{particle}} -$   
 $\chi_v|_{\text{water}}$ .

Type	Particle	$\Delta\chi_v$ <sup>49</sup>	Radius* [nm]
Paramagnetic	$\text{Mn}_2\text{O}_3$	$5.61 \times 10^{-3}$	50
	$\text{Fe}_2\text{O}_3$	$5.05 \times 10^{-3}$	30
	$\text{Co}_2\text{O}_3$	$2.91 \times 10^{-3}$	50
	$\text{CuO}$	$2.46 \times 10^{-4}$	40
Diamagnetic	$\text{Bi}_2\text{O}_3$	$-1.81 \times 10^{-5}$	40
	$\text{ZnO}$	$-1.45 \times 10^{-5}$	18

In addition, Polyethylene Glycol ( $M = 6000$  [g/mole]) was ob-  
tained from Sigma Aldrich and used as received. The nanoparti-  
cle suspensions are prepared using deionized water. Due to their  
strong magnetic properties, three different stainless steel spheres;  
420 and 440 grade (provided by Bal-tec), and 430 grade (pro-  
vided by Global Precision Ball) were used in the experiments. The  
radius of the spheres varied from 2 to 5 mm within a standard-size  
cuvette made up of polystyrene ( $12.5 \text{ mm} \times 12.5 \text{ mm} \times 45 \text{ mm}$ ).

### 2.2 Solution preparation

To improve particle stability and prevent aggregation in solution,  
we functionalize the surface of nanoparticles with polyethylene  
glycol (PEG), a widely established approach<sup>14</sup>. PEG is added at  
a concentration ten times higher than that of the nanoparticles,  
followed by a 1-hour incubation to ensure complete dispersion  
in deionized water. Afterward, the solution was homogenized  
using a vortex mixer. To further reduce the risk of aggregation,  
the solution was sonicated for 30 minutes in a bath sonicator to  
effectively disrupt any potential aggregates and promote uniform  
dispersion.

### 2.3 Magnetophoresis setup

The experimental setup for the magnetophoresis studies com-  
prises several key components as illustrated in Figure (1). A 1  
T electromagnet with pole diameters of 10 cm is used to generate  
the magnetic field. A ferromagnetic sphere is centrally positioned



136 within a cuvette, and the applied magnetic field is horizontal be-188  
137 tween the two pole pieces. The sphere is attached to a wall of the189  
138 cuvette using a glue. A high-resolution camera is mounted to cap-190  
139 ture detailed images of nanoparticle dispersion around the sphere191  
140 and within the surrounding fluid domain. Another method for192  
141 generating localized magnetic field gradients is the use of spher-193  
142 ical NdFeB permanent magnets. However, our calculations show194  
143 that the field gradients around spherical permanent magnets are195  
144 significantly smaller than those produced around a magnetized196  
145 stainless-steel sphere inside an electromagnet, resulting in weaker197  
146 magnetophoretic forces on weakly magnetic nanoparticles (see198  
147 more details below and later in Fig. S1 of the supplementary ma-199  
148 terials). Perhaps more importantly, permanent magnets present200  
149 important experimental limitations because they are always ac-201  
150 tive. As soon as the suspension is introduced into the cuvette,202  
151 particle migration begins, making it difficult to establish repro-203  
152 ducible initial conditions. In contrast, the electromagnet-based204  
153 setup allows the suspension to rest before the field is applied,205  
154 minimizing residual convective flows and enabling experiments206  
155 to start from well-defined quiescent conditions. 207

## 2.4 Particle concentration evaluation

156 To assess the spatio-temporal evolution of nano-particle concen-210  
157 tration throughout the cuvette, we first measure the averaged211  
158 light absorbance of the solution within the cuvette at various212  
159 initial concentrations ranging from 10 – 100 mg/L. As shown in213  
160 Fig. S2 of the supplementary information, the averaged nor-214  
161 malized absorbance intensity within the cuvette increases lin-215  
162 early with initial concentration indicating that the Beer-Lambert216  
163 law<sup>50,51</sup> is valid (see the supplementary materials for further dis-217  
164 cussion on the calibration curves). 218

## 2.5 Magnetization curve measurement

66 The magnetization curve of the stainless steel spheres was mea-221  
67 sured using a Vibrating Sample Magnetometer (VSM) option for222  
68 the Physical Property Measurement System (PPMS, Quantum De-223  
69 sign) at the National High Magnetic Field Laboratory. The sphere224  
170 was securely mounted on a brass trough holder using GE-7031225  
171 varnish. During the measurements, the vibration frequency was226  
172 maintained at 40 Hz, while the amplitude was adjusted between227  
173 0.2 mm and 2 mm to optimize the signal strength. 228

## 3 Multiphysics Numerical Simulations

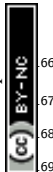
175 In addition to the detailed experiments, we performed compre-231  
176 hensive multiphysics numerical simulations. The coupled prob-232  
177 lem involves solving three key governing equations; static mag-233  
178 netic field, momentum, and mass balance, which are discussed in234  
179 detail in our previous publications<sup>42,43</sup>, and are not presented235  
180 in the main body of text for brevity but a summary of those sys-236  
181 tems of equations is provided in section II of the SI. The simu-237  
182 lations were conducted in three dimensions (3D) to capture the238  
183 full geometry and physics of the experimental setup. As shown239  
184 in Fig. 1(b), the 3D computational domain consists of a cuvette240  
185 with dimensions identical to those used in the experiments. The241  
186 magnetic pole pieces were modeled as rectangular prisms with242

dimensions specified in Fig. 1(b), separated by a 12.7 mm gap  
consistent with the experimental configuration. Although in our  
previous work<sup>42</sup>, we demonstrated that the electromagnet can  
be accurately represented in a two-dimensional axisymmetrically,  
an axisymmetric simplification is not feasible in this study due  
to the misalignment between the electromagnet and the cuvette  
axis of symmetry and the fact that the bottom and the top of the  
sphere show different magnetophoretic dynamics. Therefore, the  
pole pieces were approximated as rectangular prisms. To ensure  
that the resulting magnetic field matched that of the experimental  
electromagnet, the size of the permanent magnets was adjusted  
to generate a uniform magnetic field of 1 T around the cuvette  
(see below).

The multiphysics numerical simulations were carried out using  
the finite element method-based COMSOL Multiphysics 6.1. The  
computational domain, which includes the surrounding environ-  
ment with a radius of 2 m, was discretized into 31098 elements,  
of which 30089 were tetrahedral meshes. The batch vessel was  
resolved using 554651 elements with a maximum mesh size of  
0.5 mm. To optimize computational performance, the mesh size  
progressively increases with a maximum element growth rate of  
1.15.

## 4 Results and Discussions

Before conducting experiments involving magnetic fields and  
nanoparticle transport, we first performed a detailed character-  
ization of the sedimentation dynamics of the nanoparticles. Such  
measurements allow us to accurately assess the polydispersity of  
the nanoparticle suspension. The experimental measurements,  
presented in the Supporting Information (SI), were quantita-  
tively compared with numerical simulations and showed excellent  
agreement. The results indicate that while most particles conform  
to the vendor-specified size, a small fraction tends to form weak  
aggregates even in the absence of a magnetic field. To capture  
this polydispersity, the particle size distribution was modeled as  
 $\sum_{i=1}^3 \phi_i R_{pi}$ , where  $\phi_i$  and  $R_{pi}$  represent the volume fraction and  
radius of the  $i$ -th particle class, respectively. The fitted param-  
eters and associated data are summarized in Fig. S3 and Table I  
of the SI. In addition, to assess the particle size distributions in  
these suspensions, we performed dynamic light scattering (DLS)  
experiments. However, DLS is most sensitive to larger particles,  
and even a small number of larger particles can strongly bias the  
measured distribution and increase the particle size distribution.  
Consequently, even a relatively small population of larger parti-  
cles or aggregates can disproportionately bias the measured size  
distribution and artificially increase the apparent polydispersity.  
This limitation is particularly important for the present suspen-  
sions, where broad particle size distributions may be present.  
This will make DLS less reliable for accurately resolving the un-  
derlying primary particle size distribution. The measured hydro-  
dynamic sizes and polydispersity indices are reported in Table II  
of the Supporting Information. In contrast, the particle size dis-  
tributions obtained from the multiphysics simulations, which in-  
clude a long tail extending toward particle sizes of approximately  
150–200 nm, provide substantially better agreement with the ex-  
perimentally observed sedimentation dynamics. These inferred



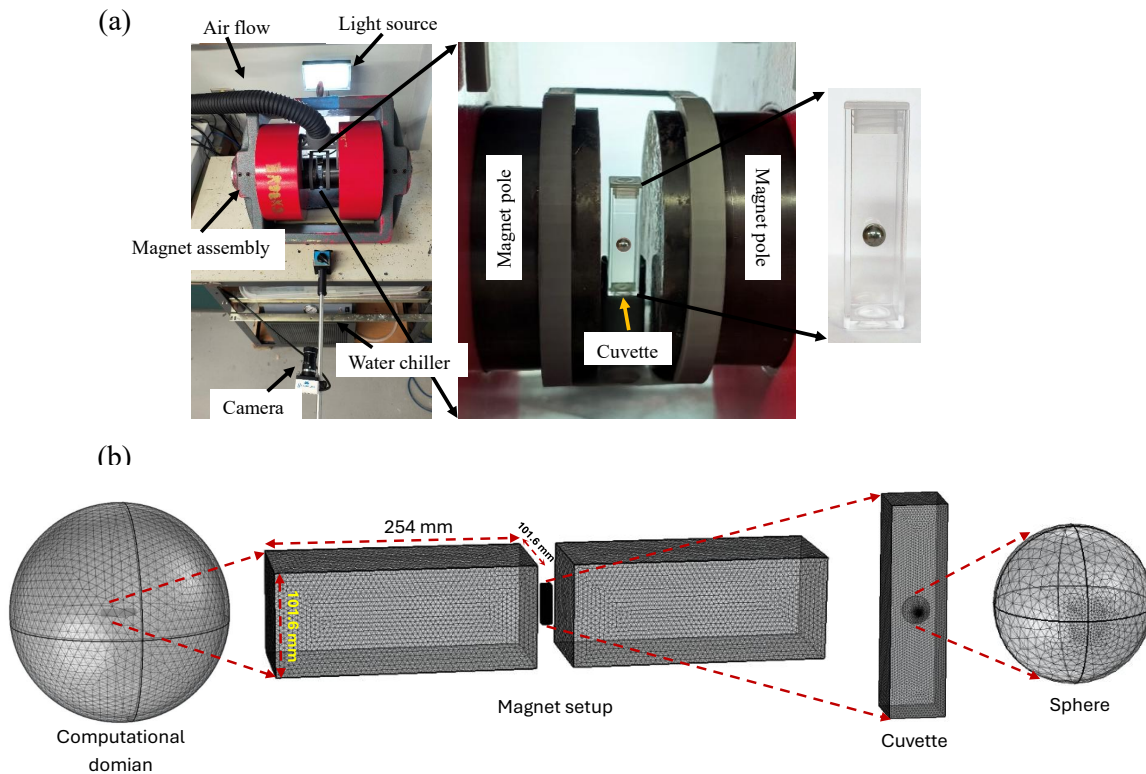


Fig. 1 (a) The top view of the experimental setup consisting of the camera, light source, electromagnet and the temperature controller. A closer view of the cuvette placed between the two flat poles is also presented in this section. (b) The computational domain along with the mesh density used for the present study.

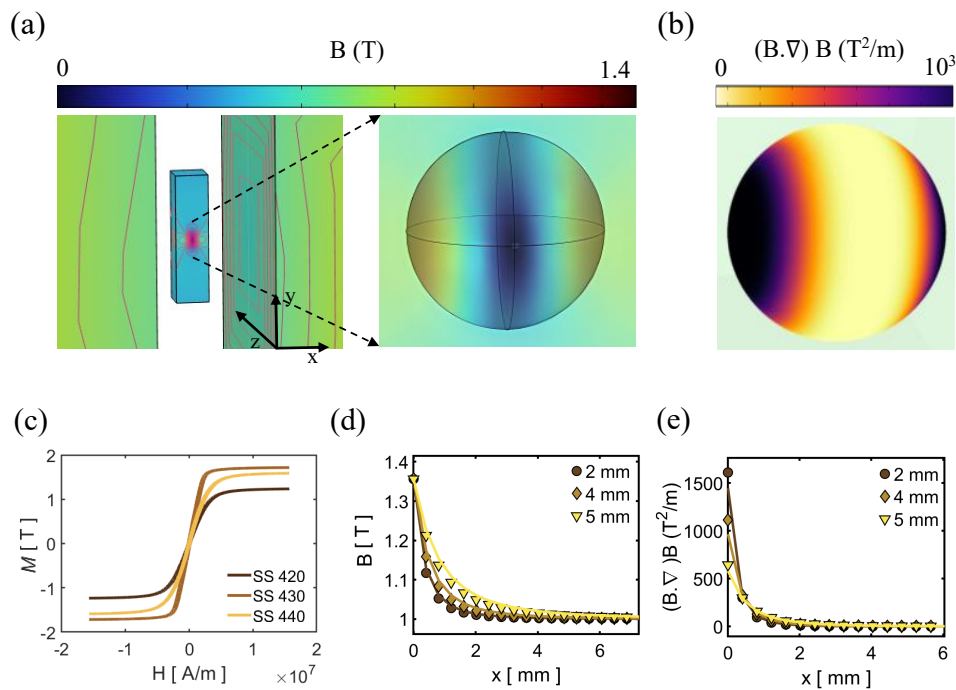


Fig. 2 Three-dimensional simulation of the magnetic flux density (a), and magnetic flux density gradients (b) around a sphere with a diameter of 5 mm under the influence of  $B_o = 1$  T applied magnetic field. The magnetic field is applied in the  $x$ -direction. (c) measured  $M$ - $H$  curves for three different grades of stainless steel spheres (420, 430 and 440). (d) Averaged magnetic flux density and (e) its gradients around sphere of different diameters under a  $B_o = 1$  T. Here, symbols represent the simulation results, while curves show theoretical predictions, where  $x = 0$  corresponds to the sphere surface.



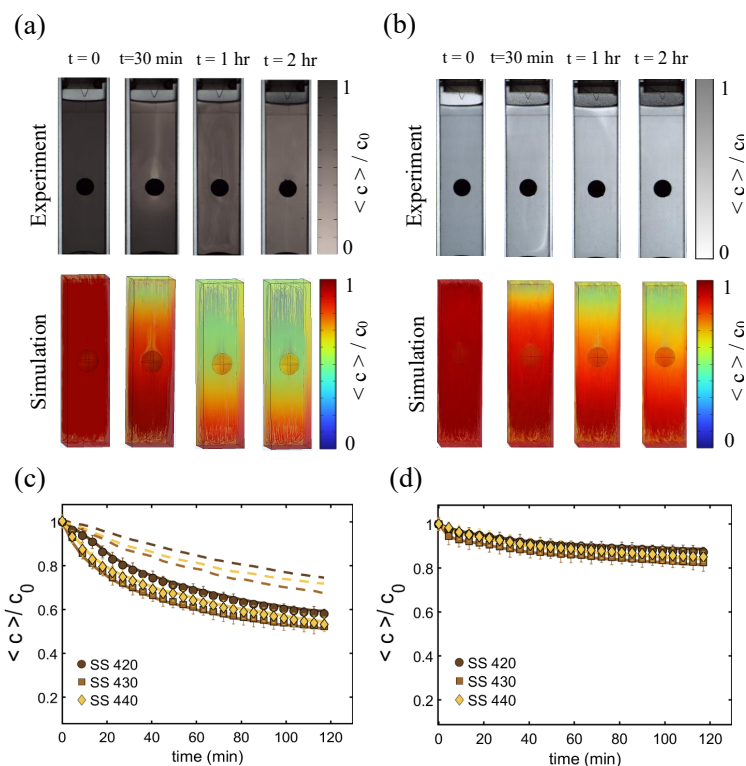


Fig. 3 The spatio-temporal evolution of (a)  $\text{Mn}_2\text{O}_3$ , and (b)  $\text{Bi}_2\text{O}_3$  nano-particle concentrations as measured in experiments at an initial concentration of 100 [mg/L], magnetic field  $\mathbf{B}_0 = 1$  [T] and sphere diameter  $d = 4$  mm (top row) and calculated through numerical simulations (bottom row). The temporal evolution of the normalized concentration of (c) manganese oxide and (d) bismuth oxide nanoparticles for different stainless steel types. The dashed lines correspond to simulation results obtained using the nanoparticle size provided by the vendor.

distributions are also generally smaller than the DLS-derived hydrodynamic sizes, which is consistent with the known tendency of DLS to overemphasize larger particles. Therefore, throughout the remainder of this manuscript, we use the particle size distributions obtained by matching the sedimentation experiments with the numerical simulations as a benchmark to compare with those particle size distributions obtained under magnetic field.

#### 4.1 Static Magnetic Field

Any magnetophoresis simulation first requires the computation of the static magnetic field, which subsequently serves as an input to the mass transport and momentum equations. Therefore, we first evaluate the spatial distribution of the magnetic field around a magnetizable sphere. Figure 2 (a,b) present the calculated magnetic flux density,  $\mathbf{B}$ , and its gradient,  $(\mathbf{B} \cdot \nabla)\mathbf{B}$ , in the vicinity of a 5 mm stainless steel (Type 430) sphere. When the external magnetic field lines intersect the sphere, the material becomes magnetized, and produces a localized enhancement in the magnetic field and a strong non-uniform field gradient. The resulting field gradient is predominantly positive near the lateral flanks of the sphere and negative along its polar regions (top and bottom). In these simulations, the experimentally measured  $M-H$  magnetization curve for stainless steel sphere (as shown in Fig. 2(c)) was incorporated. The magnetic field in the vicinity of the sphere cannot be measured accurately due to spatial resolution limits and field perturbations near the metal surface.

Therefore, to validate the numerical model, the computed magnetic field and its gradients were compared with the corresponding analytical closed-form solution<sup>52</sup>. Figure 2(d,e) show a comparison between the numerically calculated magnetic field and magnetic field gradients around the sphere and those predicted analytically. The result shows excellent agreement between the numerical results and analytical predictions, which confirm the accuracy of the magnetic field computations used in subsequent transport simulations. Since the cuvette walls are composed of non-magnetic material, they do not generate localized magnetic field gradients capable of inducing nanoparticle accumulation. As shown in the above, the externally applied magnetic field remains approximately uniform close to the cuvette walls.

#### 4.2 Magnetophoretic Dynamics

##### 4.2.1 Impact of sphere magnetization

Figure (3) shows the spatiotemporal evolution of particle concentration in a paramagnetic manganese oxide and diamagnetic bismuth oxide nanoparticle suspensions at an initial concentration of  $c_0 = 100$  mg/L, and an imposed magnetic flux density of  $\mathbf{B}_0 = 1$  T for various stainless steel spheres. Figure 3(a) shows the spatio-temporal evolution of particle concentration in experiments and simulations for paramagnetic  $\text{Mn}_2\text{O}_3$  nanoparticle solution. After applying the magnetic field, the particles start migrating towards the magnetized region of the sphere where the magnetic gradient is high. This particle migration initiates a transfer of momentum



to the fluid, giving rise to upward fluid motion in the wake of the sphere (see also movie 1 in the SI). As nanoparticles accumulate near the sphere surface, the adjacent fluid becomes increasingly depleted, resulting in localized density, and magnetic susceptibility gradients around the sphere. This imbalance generates a convective force that further drives upward flow, reinforcing the convective motion initiated by particle migration<sup>53,54</sup>. Over time, particle movement and induced fluid motion enhance transport efficiency and lead to significant particle accumulation around the sphere. As a result, the bulk concentration of the nanoparticles within the cuvette starts to decrease.

Figure 3(c) shows the temporal evolution of normalized averaged particle concentration  $\langle c \rangle / c_0$ , for paramagnetic manganese oxide nanoparticles. Here  $\langle c \rangle$  denotes the spatially averaged particle concentration at a given time, and  $c_0$  is the initial nanoparticle concentration. As shown in Figure 3(c), stainless steel-430 demonstrated slightly better separation performance than stainless steel-440, followed by stainless steel 420. Overall, the difference between various sphere types is not significant. This behavior is expected because at an applied magnetic field of 1 Tesla (or equivalently  $H = 0.796 \times 10^7$  [A/m], all spheres reached their saturation magnetization  $M_s$ . Nevertheless,  $M_{s,430} > M_{s,440} > M_{s,420}$ , and therefore, it is expected that the magnetic field gradients around these spheres follow the same trend. On the other hand, Fig. 3(b) shows the spatio-temporal evolution of normalized concentration for diamagnetic bismuth oxide particles. Fig. 3(d) shows the corresponding temporally averaged normalized concentration of diamagnetic bismuth oxide particles. For the diamagnetic particles, the type of stainless steel sphere, and the resulting magnetization does not make a significant difference on rate of particle capture. In addition, the diamagnetic particle capture around the sphere is much smaller than those of paramagnetic particles.

Following these experiments, we performed detailed multi-physics simulations using the particle size distribution obtained from sedimentation measurements. The corresponding simulation results are shown as dashed curves in Fig. 3(c,d). While these simulations agree well with the experimental concentration profiles for diamagnetic  $\text{Bi}_2\text{O}_3$  nanoparticles, they underpredict the concentration changes measured for paramagnetic  $\text{Mn}_2\text{O}_3$ . To achieve agreement with the  $\text{Mn}_2\text{O}_3$  experiments, a larger effective particle size distribution than that obtained from sedimentation is required. Table 2 summarizes the adjusted size distributions that yield the best agreement for each stainless-steel sphere type with the corresponding simulation results shown as solid curves in Fig. 3(c,d). The particle fractions  $\phi_i$  reported in Table 2, and throughout the manuscript represent effective magnetic field-dependent particle size distributions, and are assumed to be fixed over time.

Several key observations emerge. First, the inferred size distribution for  $\text{Mn}_2\text{O}_3$  shifts toward larger particle sizes, with an increased mass fraction associated with these larger aggregates compared to the no-field case (c.f. Table I in the SI). This trend suggests the presence of magnetic-field-induced aggregation and cluster formation among the paramagnetic nanoparticles. Sec-

ond, the nanoparticle size distribution remains largely insensitive to the type of stainless-steel sphere used. The conditions under which field-induced clustering becomes significant are discussed later in the manuscript. In contrast, the fitted size distribution for diamagnetic  $\text{Bi}_2\text{O}_3$  closely matches that obtained under no-field conditions, consistent with the absence of significant field-induced aggregation in diamagnetic nanoparticles.

#### 4.2.2 Competition between magnetic force and effective capture area

Another important aspect of this study is the competition between the magnetic field gradients generated around the sphere and the total surface area available for particle capture. These two factors do not scale in the same manner. As the sphere size increases, the magnetic field gradient around the sphere decreases (this is clearly shown in Fig. 2(e)), which may reduce the magnetophoretic force acting on the nanoparticles. Whereas, increasing the sphere size increases the total available surface area for nanoparticle capture. Understanding which of these opposing effects dominates is critical for the rational design of sphere-based nano-particle capture systems. To evaluate this competition, we next examine how the sphere diameter influences nanoparticle capture dynamics.

Figure 4(a) presents the temporal evolution of averaged, normalized concentration of paramagnetic manganese oxide nanoparticles for different stainless steel sphere diameters at an imposed magnet field of 1 Tesla. The results clearly indicate that the separation dynamics are significantly enhanced with increasing sphere size, as evidenced by a greater depletion of nanoparticles from the solution cell when larger spheres are used (see Fig. S4 for the corresponding spatio-temporal concentration profiles). Interestingly, the capture dynamics are initially much faster for larger spheres, and at later times (around 120 min), the total  $\text{Mn}_2\text{O}_3$  nanoparticle capture approximately doubles as sphere diameter nearly doubles. A corresponding set of experiments was performed with diamagnetic bismuth oxide ( $\text{Bi}_2\text{O}_3$ ) nanoparticles, and the results are shown in Fig. 4(b). Similar to paramagnetic particles, increasing the sphere diameter leads to a moderate enhancement in the rate of concentration depletion within the system. Diamagnetic particles preferentially accumulate near the poles of the sphere (and that is observed in our experiments), where the magnetic field is weakest.

If we consider the capture of dilute paramagnetic nanoparticles by a magnetized sphere of radius  $a$  placed in a uniform external magnetic field  $\mathbf{B}_0$ . The magnetophoretic force acting on a nano-particle is given by

$$F_m = \frac{V_p \Delta \chi_v}{\mu_0} (\mathbf{B} \cdot \nabla) \mathbf{B}, \quad (1)$$

where  $\mu_0$  is the permeability of free space,  $V_p$  is the particle volume, and  $\Delta \chi_v$  is the volume magnetic susceptibility contrast relative to the suspending fluid. On the other hand, a sphere magnetized by a uniform field behaves as a magnetic dipole with

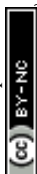


Table 2 Particle size distribution for different stainless steel simulations performed under an external magnetic field of  $\mathbf{B}_0 = 1$  T and fixed concentration  $c_0 = 100$  mg/L.

SS type	$\text{Mn}_2\text{O}_3$						$\text{Bi}_2\text{O}_3$					
	$\phi_i$			$R_{pi}$ [nm]			$\phi_i$			$R_{pi}$ [nm]		
420	0.72	0.18	0.10	150	400	700	0.77	0.13	0.10	80	120	160
430	0.72	0.18	0.10	150	500	800	0.77	0.13	0.10	80	120	160
440	0.72	0.18	0.10	150	450	750	0.77	0.13	0.10	80	120	160

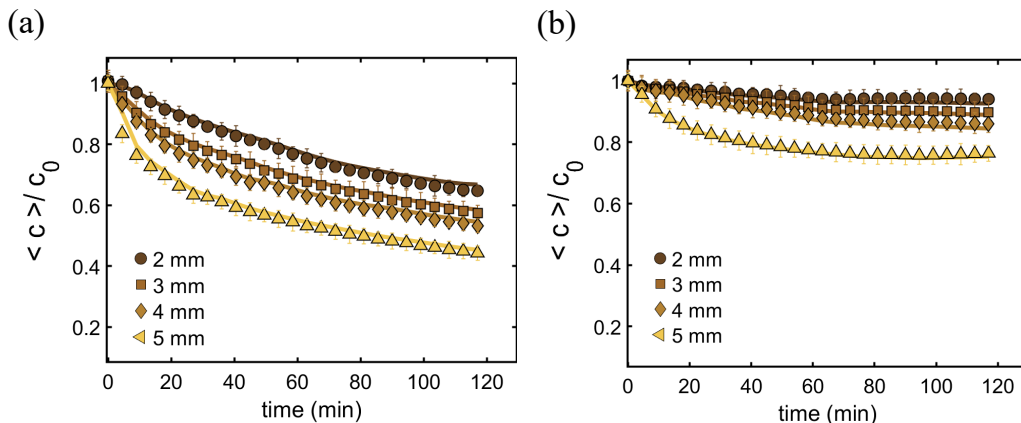


Fig. 4 The temporal evolution of normalized averaged concentration in the cuvette for (a) manganese oxide and (b) bismuth oxide nanoparticles for different stainless-steel (440) sphere diameters, at an initial concentration of 100 mg/L under a magnetic field of  $\mathbf{B}_0 = 1$  T. The solid curves denote the results of numerical simulations that are best matched to the experimental results. To better understand the above experimental results on the effect of sphere size, we developed a simple scaling analysis as follows.

a moment<sup>55</sup>

$$m \sim \frac{a^3}{\mu_0} B_0. \quad (2)$$

The magnetic field outside the sphere scales as:<sup>55</sup>

$$B(r) \sim B_0 \left( \frac{a^3}{r^3} \right) \Rightarrow B \cdot \nabla B \sim \frac{B_0^2 a^6}{r^7}. \quad (3)$$

Therefore, the magnetic force acting on a nano-particle at distance  $r$  from the sphere center scales as:

$$F_m(r) \sim \frac{V_p \Delta \chi_v}{\mu_0} \frac{B_0^2 a^6}{r^7}. \quad (4)$$

A characteristic capture radius  $r_c$  may be defined by balancing magnetic force with competing forces. As nano-particles approach the sphere due to the magnetic force, the thermal diffusion competes against it. At the capture radius, one can argue that these forces are equal to each other. As a result, in the limit of small Reynolds number and no particle-particle interactions, the magnetophoretic drift velocity can be obtained by scaling magnetic force and Stokes' drag as

$$v_{mig} \sim \frac{F_m}{6\pi\eta R_p}, \quad (5)$$

where  $\eta$  is the fluid viscosity and  $R_p$  is the nanoparticle radius. Subsequently, at the capture zone, the diffusive flux of species could be equal to the magnetophoretic flux. Balancing magnetic drift with diffusive transport (see details of analysis in SI),  $v_{mig} \sim$

$D/r_c$ , yields

$$r_c \sim a B_0^{1/3}. \quad (6)$$

Inside the capture sphere of radius  $r_c$ , the flux of nano-particles is dominated by magnetophoretic drift, and can be approximated as:

$$\Pi \sim 4\pi r_c^2 c_0 v_{mig} \sim 4\pi r_c c_0 D, \quad (7)$$

where  $c_0$  is the bulk nanoparticle concentration. Since  $r_c \sim a$ , the capture rate can be approximated as:  $\Pi \sim c_0 D a B_0^{1/3}$ . Based on the latter scaling, the flux of nano-particles scales linearly with sphere size, while to a weaker degree with the imposed magnetic field. Therefore, although increasing the sphere radius ( $a$ ) reduces the local magnetic field gradient, the geometric increase in the capture region dominates. Consequently, larger magnetized spheres are expected to enhance nano-particle capture efficiency despite weaker local gradients. The latter conclusion is consistent with experiments reported in Fig. 4(a,b).

Although the above scaling analysis provides a useful estimate, it neglects important factors such as hydrodynamic interactions between nanoparticles and fluid, nano-particle size distributions, and assumes steady flow. To obtain a more complete understanding, we performed detailed numerical simulations to quantitatively capture these effects and provide deeper insight into the experimental results. The temporal evolution of the average particle concentration was quantitatively captured using numerical simulations, and the results are shown as continuous curves in Fig. 4(a). A closer examination of the particle size distribution that provides the best agreement between experiments and sim-



Table 3 Particle size distribution for different sphere diameter simulations performed under an external magnetic field of  $\mathbf{B}_0 = 1$  T and fixed concentration  $c_0 = 100$  mg/L.

Dia. [mm]	$\text{Mn}_2\text{O}_3$						$\text{Bi}_2\text{O}_3$					
	$\phi_i$			$R_{pi}$ [nm]			$\phi_i$			$R_{pi}$ [nm]		
2	0.72	0.18	0.10	150	400	750	0.77	0.13	0.10	80	120	160
3	0.72	0.18	0.10	150	450	750	0.77	0.13	0.10	80	120	160
4	0.72	0.18	0.10	150	450	750	0.77	0.13	0.10	80	120	160
5	0.72	0.18	0.10	150	450	800	0.77	0.13	0.10	80	120	160

ulations reveals an additional aspect of the system not addressed in the preceding scaling analysis: namely, the potential for field-induced nanoparticle cluster formation. As summarized in Table 3, the application of a magnetic field induces a noticeable skew in the particle size distribution toward larger sizes for all spheres tested, resulting in an increased fraction of aggregates relative to the zero-field case (cf. Table 3 and Table I in the Supplementary Information). Notably, as the sphere diameter increases, the average particle size and fraction of larger clusters remain unchanged. These observations indicate that the enhanced magnetic capture of nanoparticles with increasing sphere diameter as reported in experiments, is not a result of field-induced clustering, but rather arises from the scaling of the total magnetic flux with sphere size ( $a$ ), as discussed in the previous analysis. The mechanisms and implications of field-induced clustering will be addressed in greater detail in subsequent sections.

To leading order, the above scaling analysis predicts that in addition to sphere size, the particle flux scales with the susceptibility contrast between the particles and the surrounding fluid, implying that the capture of diamagnetic particles should increase with sphere size, though to a significantly lesser extent than for paramagnetic nanoparticles. The latter is consistent with our experimental results shown in Fig. 4(b). Notably, our numerical simulations indicate that diamagnetic nanoparticles do not experience field-induced clustering under an applied magnetic field compared to the zero-field case. Therefore, the resulting enhancement in diamagnetic particle capture is associated with the increase in surface area of the sphere.

#### 4.2.3 Initial particle concentration

According to the above scaling analysis, initial particle concentration is expected to have a significant effect on magnetophoretic motion of nano-particles. Fig. 5(a,b) shows the temporal evolution of nano-particle concentration as a function of time for both manganese oxide (a) and bismuth oxide (b) nano-particles for an applied magnetic field of  $\mathbf{B}_0 = 1$  T. The experiments clearly demonstrate that increasing the initial concentration leads to correspondingly faster depletion of particles from the suspension. This behavior is expected: as indicated by the scaling analysis discussed above, the particle flux, and consequently the rate of concentration decay, scales linearly with the initial particle concentration. Albeit, the experimental results indicate a stronger-than-linear dependence of capture dynamics on the initial concentration of paramagnetic  $\text{Mn}_2\text{O}_3$ . For example, at 10 mg/L, the total particle capture is below 2%, whereas at  $c_0 = 100$  mg/L, it increases to approximately 60% for  $\text{Mn}_2\text{O}_3$ .

To further evaluate these observations, multiphysics simulations of particle transport were performed under an applied magnetic field of  $\mathbf{B}_0 = 1$  T. Simulations were performed and matched to the experimental results by adjusting the particle size distribution, as summarized in Table 4, and shown as continuous curves in Fig. 5(a). For the lowest concentration of 10 mg/L, the particle size distribution does not significantly change compared to no-field particle size distribution. However, achieving this agreement at higher concentrations (50 and 100 mg/L) required either an increase in the mean particle size or an enhanced mass fraction of larger particles relative to the zero-field distribution (cf. Table 4 and Table I in the SI). These findings strongly suggest that field-induced nanoparticle clustering becomes more pronounced at higher concentrations under an applied magnetic field, and that such clustering enhances the magnetic capture of paramagnetic nanoparticles. This mechanism leads to a stronger than a linear dependence of capture dynamics on the initial concentration, which is not accounted for in the scaling analysis and therefore leads to deviations from its predictions.

We next examined the behavior of diamagnetic bismuth oxide ( $\text{Bi}_2\text{O}_3$ ) nanoparticles over a range of initial particle concentrations; the results are shown in Fig. 5(b). In contrast to the paramagnetic  $\text{Mn}_2\text{O}_3$  system, the overall depletion of diamagnetic particles is substantially weaker, as expected given their much smaller negative magnetic susceptibility. Nevertheless, increasing the initial  $\text{Bi}_2\text{O}_3$  concentration results in a faster decay of the normalized particle concentration. Experimentally,  $\text{Bi}_2\text{O}_3$  nanoparticles are observed to accumulate primarily at the bottom of the cuvette due to gravitational settling, and to a lesser extent near the poles of the sphere, where the magnetic field is weakest. As the initial particle concentration increases, the extent of depletion correspondingly increases, and at long times the normalized concentration exhibits an approximately linear dependence on the initial concentration, consistent with the scaling analysis discussed above. To further interrogate these observations, numerical simulations were performed, and matched to the experimental results in a similar fashion to those reported for paramagnetic  $\text{Mn}_2\text{O}_3$  nanoparticles. The corresponding results are shown as solid curves in Fig. 5(b). Achieving quantitative agreement between experiments and simulations for diamagnetic nano-particles, only a minor increase in the volume fraction of larger particles was required (as shown Table 4 and Table I of the SI). This behavior is expected because the diamagnetic particles of bismuth oxide should not have a tendency to undergo field-induced aggregation.



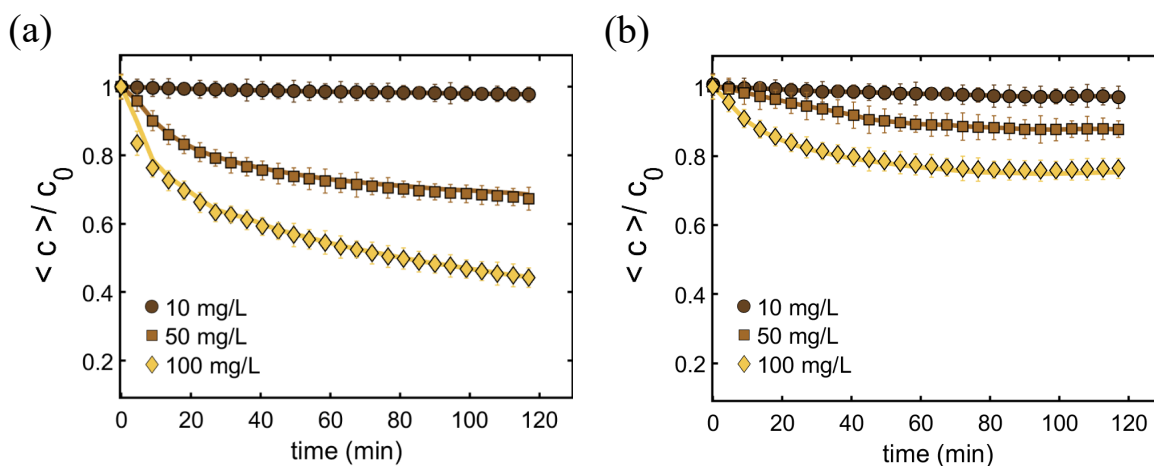


Fig. 5 Temporal evolution of normalized particle concentrations measured in experiments (symbols), and numerical simulations (solid curves) for (a) manganese oxide and (b) bismuth oxide particle at a concentration = 100 mg/L, and a magnetic field  $\mathbf{B}_0 = 1$  T and a sphere diameter  $d = 5$  nm.

Table 4 Particle size distribution for simulations performed under an external magnetic field of  $\mathbf{B}_0 = 1$  T and various initial particle concentrations.

$c_0$ [mg/L]	$\text{Mn}_2\text{O}_3$						$\text{Bi}_2\text{O}_3$					
	$\phi_i$			$R_{pi}$ [nm]			$\phi_i$			$R_{pi}$ [nm]		
10	0.82	0.10	0.08	50	150	200	0.84	0.10	0.06	40	80	120
50	0.75	0.15	0.10	100	350	500	0.80	0.12	0.08	40	80	120
100	0.72	0.18	0.10	150	450	800	0.77	0.13	0.10	80	120	160

#### 4.2.4 Effect of External Magnetic Field Strength

Next we studied the effect of an imposed magnetic field on particle capture and dynamics. The temporal evolution of normalized particle concentrations is presented in Fig. (6) for paramagnetic  $\text{Mn}_2\text{O}_3$  (a) and diamagnetic  $\text{Bi}_2\text{O}_3$  (b) suspensions. For  $\text{Mn}_2\text{O}_3$  nanoparticles, the normalized concentration decreases progressively with time, and the depletion rate increases as the magnetic field strength increases. This behavior is expected, and is due to a stronger magnetic force that particles experience as the imposed external magnetic field increases. Detailed numerical simulation results suggest that, again, similar to previous sections, a higher likelihood of field-induced particle cluster formation. The particle size distributions obtained from the simulations at different magnetic fields, summarized in Table 5, provide further evidence of field-induced cluster formation for paramagnetic nanoparticles. For  $\text{Mn}_2\text{O}_3$ , a clear shift towards larger particle sizes is observed as the magnetic field increases. At zero magnetic field, the distribution is dominated by smaller particles, whereas at  $\mathbf{B}_0 = 0.5$  T and above, the presence of larger aggregates (300-700 nm) becomes increasingly significant, accompanied by a higher mass fraction of these sizes. Fig. 6(b) shows the temporal evolution of normalized concentration for bismuth oxide nanoparticles at various imposed magnetic field. Similar to paramagnetic  $\text{Mn}_2\text{O}_3$ ,  $\text{Bi}_2\text{O}_3$  also shows a gradual increase in particle depletion from the cell. In contrast to the paramagnetic nanoparticles, the diamagnetic  $\text{Bi}_2\text{O}_3$  does not exhibit any significant forms of field-induced cluster formation as the magnetic field increases. The overall normalized concentration variation after two hours is summarized

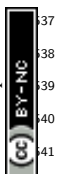
in Fig. 6(c) for both particle types. Fig. 6 (c) shows a steady increase in concentration change with field strength for  $\text{Mn}_2\text{O}_3$ , while  $\text{Bi}_2\text{O}_3$  undergoes a weaker increase in concentration variations. If we consider the total volume of the suspension outside the capture zone to be the control volume (or our system), we can write a mass balance on nanoparticles as:

$$-\Pi = \frac{d}{dt}(cV), \quad (8)$$

where  $V$  is the system volume. Rearranging this equation and integration leads to a scaling of the particle concentration change as a function of multiple parameters:

$$\frac{c_0 - c(t)}{c_0} = \frac{\Delta c}{c_0} \sim \frac{\Pi t}{V} \Rightarrow \frac{\Delta c}{c_0} \sim \left( \frac{a\Delta\chi_v^{1/6} B_0^{1/3}}{V} \right) t \quad (9)$$

The scaling prediction with respect to the applied magnetic field is shown as a dashed line in Fig. 6(c), and it underpredicts the experimental results for paramagnetic  $\text{Mn}_2\text{O}_3$  nanoparticles. Experimentally, we find that  $\Delta c/c_0 \sim B_0^{0.65}$  for  $\text{Mn}_2\text{O}_3$ , whereas for diamagnetic  $\text{Bi}_2\text{O}_3$ ,  $\Delta c/c_0 \sim B_0^{0.51}$ . This discrepancy likely arises from mechanisms not captured in the simple scaling analysis, including field-induced clustering of paramagnetic nanoparticles and magnetically driven convective flows present in both paramagnetic and diamagnetic systems. We will revisit these flow features later.



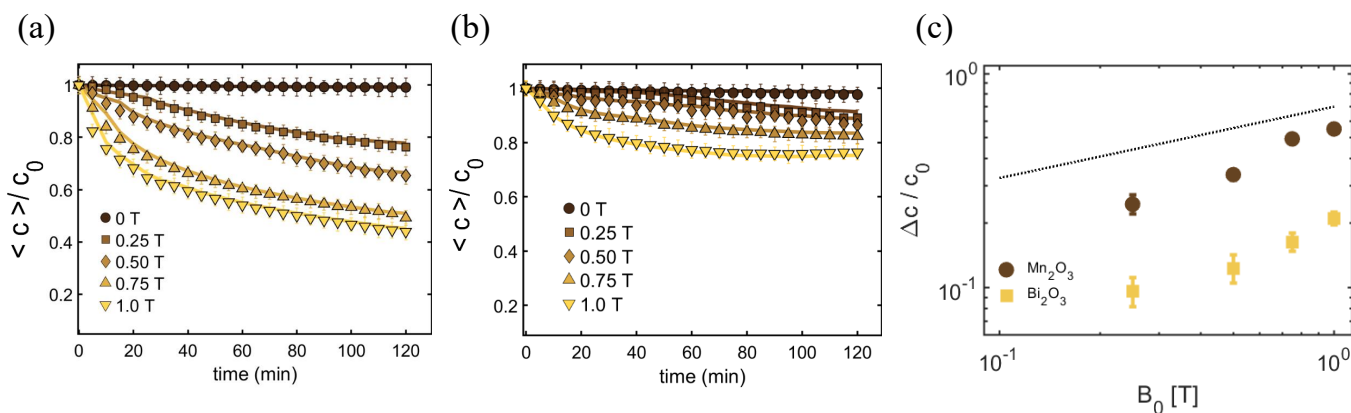


Fig. 6 Temporal evolution of normalized particle concentrations for paramagnetic  $\text{Mn}_2\text{O}_3$  (a), and diamagnetic  $\text{Bi}_2\text{O}_3$  (b) particles as a function of magnetic field strength ( $B_0$ ) with an initial concentration of 100 mg/L and a sphere diameter  $d = 5$  nm. In (a,b) symbols represent the experimental data, and the curves represent the simulation results that best match the experiments. (c) The normalized concentration change as a function of the imposed magnetic field after a 2-hour period for both paramagnetic (circles) and diamagnetic particles (squares). The dashed line in part (c) corresponds to the prediction of the scaling analysis.

Table 5 Particle size distribution for simulations performed at a fixed concentration  $c_0 = 100$  mg/L.

Magnetic field [T]	$\text{Mn}_2\text{O}_3$					$\text{Bi}_2\text{O}_3$						
	$\phi_i$			$R_{pi}$ [nm]		$\phi_i$			$R_{pi}$ [nm]			
0	0.80	0.10	0.10	50	150	200	0.80	0.12	0.08	80	120	160
0.25	0.78	0.12	0.10	100	250	400	0.78	0.12	0.10	80	120	160
0.5	0.75	0.15	0.10	150	350	500	0.78	0.12	0.10	80	120	160
0.75	0.72	0.18	0.10	150	400	700	0.78	0.12	0.10	80	120	160
1	0.72	0.18	0.10	150	450	800	0.77	0.13	0.10	80	120	160

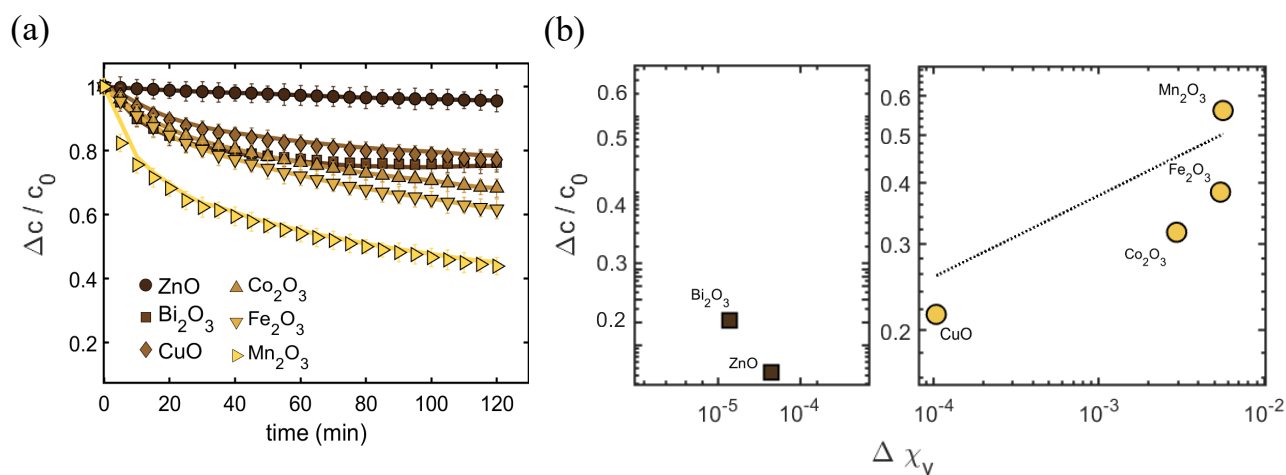
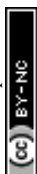


Fig. 7 Temporal evolution of normalized particle concentrations for all the paramagnetic and diamagnetic nanoparticles considered in this study with an initial concentration of 100 mg/L,  $B_0 = 1$  T and a sphere diameter  $d = 5$  nm. Here, the symbols represent the experimental data, and the solid curves represent the simulation results that best match the experiments. (b) Normalized change in concentration as a function of magnetic susceptibility  $\Delta \chi_v$ .

Table 6 Particle size distributions used in simulations under external magnetic fields of  $B_0 = 0$  T and  $B_0 = 1$  T for evaluating the effect of magnetic susceptibility.

Material	$B_0 = 0$ T					$B_0 = 1$ T						
	$\phi_i$			$R_{pi}$ [nm]		$\phi_i$			$R_{pi}$ [nm]			
ZnO	0.84	0.10	0.06	18	36	54	0.82	0.10	0.08	18	36	54
CuO	0.84	0.10	0.06	40	80	120	0.76	0.14	0.10	80	160	400
$\text{Co}_2\text{O}_3$	0.82	0.10	0.08	50	100	150	0.74	0.14	0.12	100	200	450
$\text{Fe}_2\text{O}_3$	0.82	0.10	0.08	60	90	150	0.74	0.14	0.12	120	270	630



#### 4.2.5 Magnetic susceptibility

Finally, we return to the impact of nanoparticle magnetic susceptibility. Figure 7(a) shows the temporal evolution of particle concentration for various nano-particle types under a magnetic field  $\mathbf{B}_0 = 1$  T,  $c_0 = 100$  mg/L and the sphere diameter  $d = 5$  mm. Paramagnetic particles (manganese, cobalt, iron, copper) exhibit a continuous decrease in bulk concentration over time, indicating effective particle capture around the magnetized sphere. Among the diamagnetic materials, bismuth oxide exhibits a notable change in concentration, indicating measurable repulsion from the high-gradient region, whereas zinc oxide shows only a weak response due to its comparatively small magnetic susceptibility. Fig. 7(b) presents the normalized change in particle concentration,  $\Delta c/c_0$ , after two hours as a function of magnetic susceptibility  $\Delta\chi_v$  for all nanoparticles considered in this study. For paramagnetic nanoparticles,  $\Delta c/c_0$  increases strongly with magnetic susceptibility, with manganese oxide exhibiting the largest concentration change, followed by iron oxide, while cobalt oxide and copper oxide show comparatively weaker magnetophoretic capture. The dashed line in Fig. 7(b) represents the scaling predicted by Eq. (9). Although the scaling captures the general trend at low magnetic susceptibility, it underpredicts the experimentally observed dependence at higher susceptibilities. To elucidate the discrepancy between the experiments and the scaling analysis, we performed detailed numerical simulations of particle transport. The best agreement with experiments is shown as solid curves in Fig. 7(a). The corresponding particle size distributions, both in the absence of a magnetic field and under an applied field of 1 T, are summarized in Table 6. The results indicate that paramagnetic particles form larger clusters in the presence of a magnetic field, with iron and copper oxides reaching effective sizes exceeding 500 nm. This growth substantially enhances the magnetic force acting on the clusters, thereby accelerating their magnetophoretic capture to the sphere. Such field-induced clustering likely accounts for the discrepancy between the scaling predictions and the experimental trends observed in Fig. 7(b). In contrast, diamagnetic zinc oxide shows no evidence of field-induced clustering, consistent with its comparatively weak response.

#### 4.3 Field-induced cluster formation

Our numerical simulations suggest that the paramagnetic nanoparticles may undergo field-induced cluster formation near the sphere under certain operating conditions such as initial concentration, applied magnetic field, and particle magnetic susceptibility. It is well established in the prior literature that magnetic particles can self-assemble and undergo field-induced cluster formation<sup>56,57</sup>. Prior literature have advanced theoretical and experimental aspects and illustrated that under a uniform magnetic field, two dimensionless quantities can describe the threshold for onset of field-induced cluster formation<sup>58,59</sup>. These dimensionless numbers include the magnetic coupling parameter  $\Gamma$  and the aggregation parameter  $N^*$ . The coupling parameter  $\Gamma$  expresses the competition between magnetic dipolar energy and thermal agitation. Under an externally imposed magnetic field, magnetic nanoparticles develop induced magnetic dipoles and

through dipole–dipole interactions, experience attractive forces that promote field-induced aggregation and cluster formation. The strength of these interactions is commonly characterized by the dimensionless interaction parameter  $\Gamma$ , defined as<sup>31</sup>:

$$\Gamma = \frac{\pi\Delta\chi^2 B^2 R_p^3}{9\mu_o k_B T}. \quad (10)$$

The aggregation parameter  $N^*$ , reflects the role of particle concentration in promoting collective behavior and is expressed as:

$$N^* = \sqrt{\phi_o e^{\Gamma-1}}. \quad (11)$$

Here,  $\phi_o$  is the volume fraction of the nanoparticles in the solution. It has been demonstrated through both experiments and theoretical studies that under a uniform magnetic field, field-induced cluster formation occurs for conditions that satisfy  $\Gamma > 1$  and  $N^* > 1$ . Although in our experiments the magnetic field around sphere is highly non-uniform, these dimensionless numbers offer a reasonable first-order assessment of field-induced cluster formation.

Figure (8) present a series of phase diagrams showing the variation of the coupling parameter  $\Gamma$  (a,c) and the aggregation parameter  $N^*$  (b,d) as functions of particle radius ( $R_p$ ) and applied magnetic field strength ( $\mathbf{B}_0$ ). Panels (a,b) correspond to various initial concentration of  $\text{Mn}_2\text{O}_3$  nanoparticles, whereas panels (c,d) represent other nanoparticles when magnetic susceptibility is varied. The solid curves denote the threshold conditions  $\Gamma = 1$  and  $N^* = 1$ , which together define the necessary criterion for the onset of field-induced cluster formation. Regions beyond these threshold curves correspond to parameter combinations for which clustering is expected, while clustering is not anticipated below the thresholds.

As shown in Fig. 8(a,b), decreasing the initial concentration of  $\text{Mn}_2\text{O}_3$  nanoparticles shifts the onset of cluster formation toward larger particle radii and higher magnetic field strengths. At an initial concentration of 10 mg/L, the predicted thresholds for clustering occur at particle sizes and magnetic fields that lie well beyond the experimental conditions used in this study. Consequently, field-induced cluster formation is not expected under these conditions, consistent with the magnetophoresis experiments and numerical simulations discussed above in Fig. (5). Conversely, at higher initial concentrations, the predicted onset of field-induced clustering falls within the experimentally accessible ranges of particle size and magnetic field strength. Under these conditions, the analysis predicts the formation of magnetic-field-induced particle clusters, in agreement with the experimental observations and numerical simulation results reported earlier in Fig. (5).

While, the above discussion provides a valuable theoretical criterion for predicting the onset of clustering as a function of initial concentrations, our experiments with  $\text{Mn}_2\text{O}_3$ , at an initial concentration of 100 mg/L and various imposed magnetic fields ( $\mathbf{B}_0$ ; as shown in Fig. (6)) suggest that field-induced cluster formation exists at a considerably lower magnetic field ( $\mathbf{B}_0 \sim 0.25$  T), than what this framework predicts (which is for



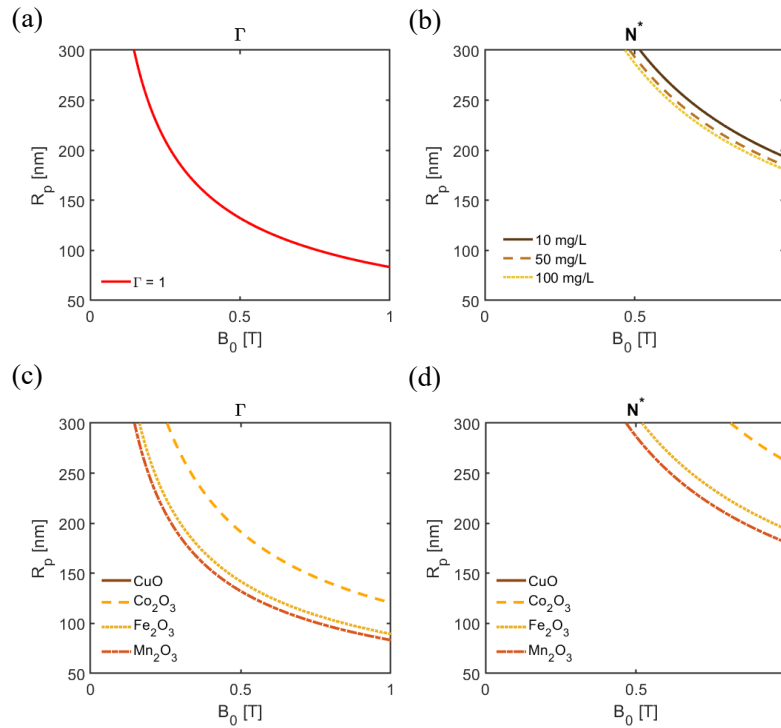


Fig. 8 Plot of  $\Gamma$  (a) and  $N^*$  (b) are presented as functions of particle size  $R_p$  and magnetic field  $\mathbf{B}_0$  for  $\text{Mn}_2\text{O}_3$  nanoparticles at different initial concentrations ( $c_0 = 10, 50,$  and  $100$  mg/L). (c, d) denote  $\Gamma$  and  $N^*$  for nanoparticles with different magnetic susceptibilities and initial concentration of  $100$  mg/L. The curves highlight the points where  $\Gamma = 1$  and  $N^* = 1$ . Note that within the range of particle size and applied magnetic fields, CuO is not expected to reach the thresholds of  $\Gamma = 1$  or  $N^* = 1$ .

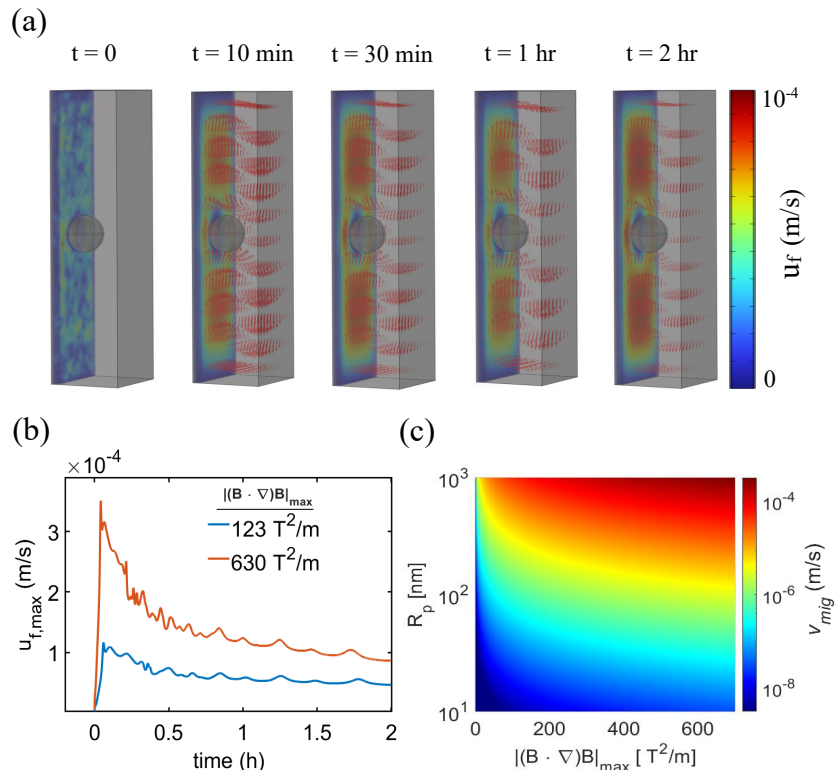


Fig. 9 (a) Spatio-temporal evolution of velocity vectors and velocity magnitude for paramagnetic  $\text{Mn}_2\text{O}_3$  nanoparticles at  $c_0 = 100$  mg/L and  $\mathbf{B}_0 = 1$  T. (b) Temporal evolution of the maximum fluid velocity at the lowest and highest magnetic field strength used in this study. (c) Magnetophoretic particle velocity as a function of particle size and magnetic field gradient calculated for paramagnetic  $\text{Mn}_2\text{O}_3$  nanoparticles at  $c_0 = 100$  mg/L.



$\mathbf{B}_0 > 0.75$  T). The model that relies on the thresholds for  $\Gamma - N^*$  assumes a uniform magnetic field. However, in this study, the magnetic field around the magnetized sphere is extremely non-uniform. The non-uniform magnetic field may (i) directly increase magnetophoretic drift and hence collision frequency between particles, and/or (ii) induce weak but finite fluid flows through particle-fluid coupling. The latter effect will be discussed in detail below. Eventually, these two effects are expected to further enhance transport and association of particles towards cluster formation.

Figure 8(c,d) illustrates the onset of field-induced clustering for nanoparticles with varying magnetic susceptibilities at an initial concentration of 100 mg/L. Based on these two dimensionless parameters ( $\Gamma - N^*$ ), increasing magnetic susceptibility promotes cluster formation at smaller particle sizes and/or lower applied magnetic fields. Accordingly, for CuO, clustering is not expected within the range of particle sizes and magnetic fields considered in Fig. 8 (For this reason, the curve associated with this nanoparticle can not be seen in the range of parameters reported in Fig. 8(c,d)). However, the magnetophoretic experiments and simulations in Fig. 7(a) indicate that even this weakly paramagnetic nanoparticle exhibits modest field-induced clustering at  $\mathbf{B}_0 = 1$  T. For the remaining nanoparticles, the dimensionless parameters exceed unity over the relevant range of particle sizes and magnetic fields, suggesting that clustering should occur under an applied field of 1 T according to the  $\Gamma - N^*$  framework, and that is consistent with our magnetophoresis experiments and simulations on those nano-particles. The discrepancy observed for CuO may arise from the non-uniformity of the magnetic field, as discussed above.

#### 4.4 Field-induced Convective Flows

An important aspect of this study that has not yet been discussed in detail is the role of field-induced convective flows. These flows are expected to arise from the coupling between magnetophoretic nanoparticle motion and the surrounding fluid. As nanoparticles migrate under the influence of a non-uniform magnetic field, they transfer momentum to the fluid, which in turn should generate convective flows. In this part, we quantify this effect and its role in transport of nanoparticles. Figure 9(a) shows the computed fluid velocity vectors and velocity magnitude around a sphere for a suspension containing 100 mg/L  $\text{Mn}_2\text{O}_3$  nanoparticles, subjected to an imposed magnetic field  $\mathbf{B}_0 = 1$  T and a sphere diameter of 5 mm. Shortly after the onset of flow, the fluid velocity increases rapidly, reaching a maximum before gradually decreasing and approaching a steady value. To quantify this temporal behavior, Fig. 9(b) presents the temporal evolution of the maximum fluid velocity  $u_{f,max}$  within the computational domain at the lowest and highest magnetic field gradients used in this study that correspond to  $\mathbf{B}_0 = 0.25$  T and  $\mathbf{B}_0 = 1.0$  T. At the lower field gradient of 123  $\text{T}^2/\text{m}$ , the induced flow increases rapidly to a maximum velocity of  $\approx 0.1$  mm/s before gradually decaying, whereas at the higher field gradient

of 630  $\text{T}^2/\text{m}$  the maximum velocity exceeds  $\approx 0.3$  mm/s with a similar transient behavior. For both cases, the fluid velocity decays quickly and approaches a nearly constant value at longer times. This overshoot can be rationalized by considering the evolution of particle concentration near the sphere surface with a high field gradient as follows. At  $t = 0$  for both cases, the suspension is spatially uniform, resulting in negligible driving forces for fluid motion. As particles undergo magnetophoretic motion and are captured by the sphere, concentration gradients emerge, which in turn initiates magnetically driven convection. The establishment of a concentration gradient enhances the local driving force, producing a maximum in  $u_{f,max}$ . With continued depletion, the overall concentration of particles in the domain decreases, and the concentration gradients weaken. The latter leads to a gradual reduction in the induced velocity. Fig. 9 (b) presents the calculated magnetophoretic particle velocity,  $v_{mig}$  as a function of particle radius,  $R_p$  and magnetic field gradients. The  $v_{mig}$  increases monotonically with both  $R_p$  and  $(\mathbf{B} \cdot \nabla)\mathbf{B}$ , with larger particles experiencing orders-of-magnitude higher velocities compared to smaller counterparts. Notably, the maximum fluid velocities  $u_{f,max}$  obtained from the fully coupled simulations significantly exceed the corresponding magnetophoretic particle velocities of the particle or  $v_{mig}$  under an otherwise similar particle and magnetic field conditions. This disparity provides strong evidence for the emergence of field-induced convective flows arising from momentum transfer between migrating nanoparticles and the surrounding fluid. Such flows are expected to enhance particle transport and promote more efficient separation and capture. To verify this, we performed additional simulations in which fluid flow was neglected (not solved for, and it is assumed that  $u_f = 0$ ) and only particle transport was considered; the results are shown in Fig. S5 of the SI. The comparison clearly demonstrates that fluid-particle interactions significantly enhance the magnetophoretic capture of paramagnetic nanoparticles.

To further evaluate the formation of this induced convective flows and by drawing an analogy between natural convection and magnetic field-induced convective flows, a dimensionless magnetic Grashof number appears. The magnetic Grashof number  $Gr_m$  characterizes the relative importance of the magnetically induced body forces and viscous forces in the system, and can be defined as:<sup>42</sup>

$$Gr_m = \frac{\rho \Delta \chi_m |c_s - c_\infty| L^3 |(\mathbf{B} \cdot \nabla)\mathbf{B}|}{M_i (1 + \chi_{v,f}) \mu_0 \eta^2}, \quad (12)$$

Here,  $\rho$  is the density of the magnetic particles, taken as for  $\text{Mn}_2\text{O}_3 = 5.03$  g/cm<sup>3</sup>,  $\text{Fe}_2\text{O}_3 = 5.24$  g/cm<sup>3</sup>,  $\text{Co}_2\text{O}_3 = 5.18$  g/cm<sup>3</sup>, and  $\text{CuO} = 6.31$  g/cm<sup>3</sup>,  $\Delta \chi_m$  is the molar magnetic susceptibility of the nanoparticles,  $c_0$  represents the concentration of the particles and  $c_\infty$  is the the concentration of the surrounding medium. The parameter  $L$  is the critical length, which is cuvette width, and  $M_i$  is the molar mass of nanoparticle  $i$ , and  $\chi_{v,f}$  ( $-9.07 \times 10^{-6}$ ) is the volume magnetic susceptibility of the surrounding fluid. The permeability of free space is given by  $\mu_0$ , and  $\eta = 1 \times 10^{-3}$  Pa.s is



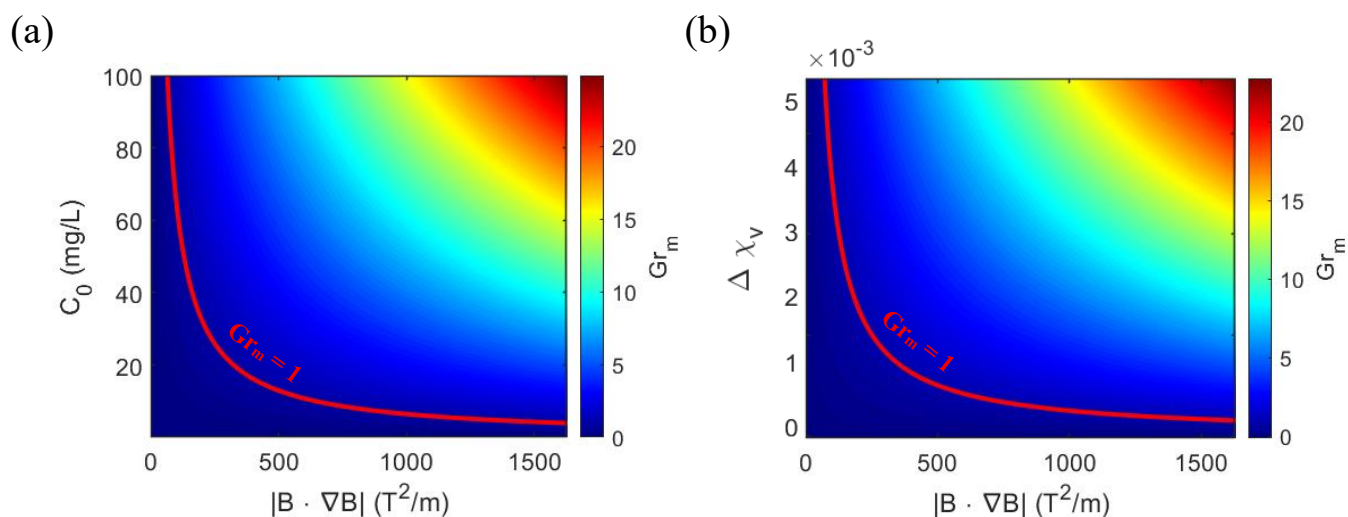


Fig. 10 Map of magnetic Grashof number as a function of initial concentration and field gradients for  $\text{Mn}_2\text{O}_3$  nanoparticles at  $c_0 = 100$  mg/L. (b) Magnetic Grashof number as a function of magnetic field gradient and magnetic susceptibility  $\Delta\chi_v$ .

the dynamic viscosity of the fluid.

Figure 10 (a) presents the heat map of the magnetic Grashof number  $Gr_m$  as a function of initial concentration and magnetic field gradients for paramagnetic  $\text{Mn}_2\text{O}_3$  nanoparticles. Beginning with  $\text{Mn}_2\text{O}_3$  nanoparticles and initial concentration of 10 mg/L, at very low values of  $(\mathbf{B} \cdot \nabla)\mathbf{B}$  up to 600  $\text{T}^2/\text{m}$ ,  $Gr_m$  remains less than unity, indicating that the magnetically driven fluid motion is too weak. As initial concentration of  $\text{Mn}_2\text{O}_3$  nanoparticles increase, especially for 50 and 100 mg/L, it is expected that field-induced convective flows to exist for  $(\mathbf{B} \cdot \nabla)\mathbf{B} > 100 - 200$   $\text{T}^2/\text{m}$  values. Indeed this is consistent with our experiments that clearly show formation of field-induced convective flows (see movie 1 in the SI).

Figure 10 (b) shows the plot of magnetic Grashof number as a function of magnetic susceptibility and field gradients for an initial particle concentration of 100 mg/L. Based on these calculations, for paramagnetic  $\text{Mn}_2\text{O}_3$  nanoparticles with  $\Delta\chi_v = 5.6 \times 10^{-3}$ , it is expected that field-induced convective flows to be present for  $|\mathbf{B} \cdot \nabla\mathbf{B}| > 200$   $\text{T}^2/\text{m}$ , which is consistent with our experiments showing clear convective flows at higher field gradients. As magnetic susceptibility of the nanoparticle decreases, it is expected that onset of secondary flows to shift to higher field gradients. Under the conditions corresponding to Fig. 7(a), where  $|\mathbf{B} \cdot \nabla\mathbf{B}|_{\text{max}} \approx 630$   $\text{T}^2/\text{m}$ , only  $\text{Fe}_2\text{O}_3$  and  $\text{Co}_2\text{O}_3$  are expected to exhibit field-induced convective flows. This prediction is consistent with our magnetophoresis experiments, which show clear evidence of such flows for  $\text{Fe}_2\text{O}_3$  and  $\text{Co}_2\text{O}_3$ , but minimal response in the case of  $\text{CuO}$  (see Fig. S6 in the Supporting Information).

## 5 Summary and Conclusions

In this study, we investigated the magnetophoretic transport and capture of nanoparticles over a broad range of magnetic susceptibilities (e.g.,  $\text{Bi}_2\text{O}_3$ ,  $\text{ZnO}$ ,  $\text{CuO}$ ,  $\text{Co}_2\text{O}_3$ ,  $\text{Fe}_2\text{O}_3$ , and  $\text{Mn}_2\text{O}_3$ ), ini-

tial particle concentration (10-100 mg/L), imposed magnetic field (0-1 T), and magnetic field gradients (0-1500  $\text{T}^2/\text{m}$ ) through a combination of experiments, scaling analysis, and multiphysics simulations. The results reveal that nanoparticle capture in non-uniform magnetic fields is governed by a complex interplay of magnetic forces, particle-particle interactions, and fluid-particle coupling.

For paramagnetic nanoparticles, enhanced capture is driven by magnetic-field-induced clustering, which increases effective particle size and amplifies magnetic forces. The extent of clustering grows with magnetic susceptibility, field strength, and initial concentration, leading to a strongly nonlinear dependence of magnetophoretic dynamics. In contrast, diamagnetic nanoparticles show negligible clustering and largely follow scaling predictions.

The onset of field-clustering is reasonably described by the  $\Gamma$ - $N^*$  framework, although deviations arise due to the highly non-uniform magnetic field used in this study. This highly non-uniform magnetic field around the sphere promotes aggregation at lower field strengths. In addition, simulations reveal the presence of field-induced convective flows arising from particle-fluid momentum transfer. These flows significantly enhance transport and capture, as confirmed by comparisons with simulations that neglect fluid motion.

Finally, increasing sphere size enhances capture efficiency despite weaker local field gradients due to the expansion of the effective capture region. Overall, the results demonstrate that magnetophoretic capture of nano-particles is governed by coupled effects of clustering and fluid motion, which highlight the limitations of classical scaling and provide guidance for the design of magnetic separation systems. The present study focuses on magnetized spherical geometry, however, alternative magnetic geometries capable of generating stronger localized magnetic-field gradients, such as sharp-edge collectors, corners, or optimized multi-collector configurations, may further enhance clustering, convective transport, and nanoparticle capture. Investi-



gation of such geometries represents an important direction for  
future studies.

## 6 Acknowledgments

This work was performed at the National High Magnetic Field  
Laboratory, which is supported by the National Science Founda-  
tion Cooperative Agreement No. DMR-1644779 and the State of  
Florida. This work was supported by the Center for Rare Earths,  
Critical Minerals, and Industrial Byproducts, through funding  
provided by the State of Florida.

## References

- S. Li, M. Wang, Z. Zhu, Q. Wang, X. Zhang, H. Song and D. Cang, *Separation and purification technology*, 2012, **84**, 56–62.
- D. Kelland, *IEEE Transactions on Magnetism*, 1973, **9**, 307–310.
- S. S. Leong, S. P. Yeap and J. Lim, *Interface focus*, 2016, **6**, 20160048.
- J.-Y. Tseng, C.-C. Chang, C.-W. Tu, M.-H. Yuan, C.-Y. Chang, C.-F. Chang, Y.-H. Chen, J.-L. Shie, D.-R. Ji, B.-L. Liu *et al.*, *Processes*, 2023, **11**, 965.
- J. A. Ritter, A. D. Ebner, K. D. Daniel and K. L. Stewart, *Journal of Magnetism and Magnetic Materials*, 2004, **280**, 184–201.
- V. Rizos, E. Righetti and A. Kassab, *Energy Reports*, 2024, **12**, 1673–1682.
- Z. Cherkezova-Zheleva, M. Burada, A. E. Sobetkii, D. Paneva, S. A. Fironda and R.-R. Piticescu, *Metals*, 2024, **14**, 658.
- D. Teng, J. Wu, Q. Ma, W. Wang, G. Zhou, G. Fan, Y. Cao and P. Li, *ACS omega*, 2024, **10**, 76–92.
- F. Liu, C. Peng, A. Porvali, Z. Wang, B. P. Wilson and M. Lundstrom, *ACS Sustainable Chemistry & Engineering*, 2019, **7**, 16103–16111.
- F. Deng, H. Olvera-Vargas, M. Zhou, S. Qiu, I. Sirés and E. Brillias, *Chemical Reviews*, 2023, **123**, 4635–4662.
- G. Zante, C. E. Elgar, J. M. Hartley, R. Mukherjee, J. Kettle, L. E. Horsfall, A. Walton, G. D. Harper and A. P. Abbott, *RSC Sustainability*, 2024, **2**, 320–347.
- A. Akthakul, A. I. Hochbaum, F. Stellacci and A. M. Mayes, *Advanced Materials*, 2005, **17**, 532–535.
- Y. A. Kahnouji, E. Mosaddegh and M. A. Bolorizadeh, *Materials Science and Engineering: C*, 2019, **103**, 109817.
- S. Shrestha, B. Wang and P. Dutta, *Advances in colloid and interface science*, 2020, **279**, 102162.
- B. Lake, T. Siegrist, T. E. Albrecht, H. Mohammadigoushki, M. Humayun and J. Ali, *Industrial & Engineering Chemistry Research*, 2025, **64**, 19781–19796.
- Z. Hu, D. Lu, X. Zheng, Y. Wang, Z. Xue and S. Xu, *Powder Technology*, 2023, **421**, 118435.
- W. Ge, A. Encinas, E. Araujo and S. Song, *Results in physics*, 2017, **7**, 4278–4286.
- J. Svoboda, *Magnetic techniques for the treatment of materials*, Springer Science & Business Media, 2004.
- C. T. Yavuz, J. Mayo, W. W. Yu, A. Prakash, J. C. Falkner, S. Yean, L. Cong, H. J. Shipley, A. Kan, M. Tomson *et al.*, *science*, 2006, **314**, 964–967.
- L. Chen, Y. Wu, N. T. H. Nhung, C. He, H. Chen, G. Dodbiba, A. Otsuki and T. Fujita, *Metals*, 2023, **13**, 241.
- J. Watson, *IEEE Transactions on Magnetism*, 1975, **11**, 1597–1599.
- J. H. Watson, *Journal of Applied Physics*, 1973, **44**, 4209–4213.
- M. Iranmanesh and J. Hulliger, *Chemical Society Reviews*, 2017, **46**, 5925–5934.
- A. Ditsch, S. Lindenmann, P. E. Laibinis, D. I. Wang and T. A. Hatton, *Industrial & Engineering Chemistry Research*, 2005, **44**, 6824–6836.
- G. D. Moeser, K. A. Roach, W. H. Green, T. Alan Hatton and P. E. Laibinis, *AIChE Journal*, 2004, **50**, 2835–2848.
- J. Svoboda, *Magnetic techniques for the treatment of materials*, Springer Science & Business Media, 2004.
- S. S. Leong, Z. Ahmad, S. C. Low, J. Camacho, J. Farauo and J. Lim, *Langmuir*, 2020, **36**, 8033–8055.
- S. S. Leong, Z. Ahmad and J. Lim, *Soft Matter*, 2015, **11**, 6968–6980.
- J. Lim, S. P. Yeap and S. C. Low, *Separation and Purification Technology*, 2014, **123**, 171–174.
- V. Schaller, U. Kräling, C. Rusu, K. Petersson, J. Wipenmyr, A. Krozer, G. Wahnström, A. Sanz-Velasco, P. Enoksson and C. Johansson, *Journal of Applied Physics*, 2008, **104**, 093918.
- G. De Las Cuevas, J. Farauo and J. Camacho, *The Journal of Physical Chemistry C*, 2008, **112**, 945–950.
- M. Klokkenburg, R. P. Dullens, W. K. Kegel, B. H. Erné and A. P. Philipse, *Physical review letters*, 2006, **96**, 037203.
- M. Klokkenburg, B. H. Erné, J. D. Meeldijk, A. Wiedenmann, A. V. Petukhov, R. P. Dullens and A. P. Philipse, *Physical review letters*, 2006, **97**, 185702.
- V. Socoliuc, L. Vékás and R. Turcu, *Soft Matter*, 2013, **9**, 3098–3105.
- J. M. Laskar, J. Philip and B. Raj, *Physical Review E—Statistical, Nonlinear, and Soft Matter Physics*, 2010, **82**, 021402.
- G. P. Gajula, M. T. Neves-Petersen and S. B. Petersen, *Applied Physics Letters*, 2010, **97**, 103103.
- H. Ezzaier, J. Alves Marins, I. Razvin, M. Abbas, A. Ben Haj Amara, A. Zubarev and P. Kuzhir, *The Journal of chemical physics*, 2017, **146**, 114902.
- J. S. Andreu, J. Camacho and J. Farauo, *Soft Matter*, 2011, **7**, 2336–2339.
- J. Farauo, J. S. Andreu and J. Camacho, *Soft Matter*, 2013, **9**, 6654–6664.
- A. Işıldar, E. D. van Hullebusch, M. Lenz, G. Du Laing, A. Marra, A. Cesaro, S. Panda, A. Akcil, M. A. Kucuker and K. Kuchta, *Journal of hazardous materials*, 2019, **362**, 467–481.
- K. H. Chan, J. Anawati, M. Malik and G. Azimi, *ACS Sustainable Chemistry & Engineering*, 2021, **9**, 4398–4410.
- P. Rassolov, J. Ali, T. Siegrist, M. Humayun and H. Mohammadigoushki, *Physical Review Fluids*, 2025, **10**, 073701.



- 967 43 M. B. Khan, P. Rassolov, J. Ali, T. Siegrist, M. Humayun  
968 and H. Mohammadigoushki, *The Journal of Chemical Physics*,  
969 2025, **163**, year.
- 970 44 S. Araj, C. A. Moyer, R. Aidun and E. Matijevic, *Journal of*  
971 *Applied Physics*, 1985, **57**, 4286–4288.
- 972 45 M. Haque, R. Aidun, C. Moyer and S. Araj, *Journal of Applied*  
973 *Physics*, 1988, **63**, 3239–3240.
- 974 46 F. Friedlaender, R. Gerber, H.-P. Henkel and R. Birss, *IEEE*  
975 *Transactions on Magnetics*, 2003, **17**, 2804–2806.
- 976 47 L. A. Romo, A. López-Fernández, I. García-Díaz, P. Fernández,  
977 A. Urbieto and F. A. López, *RSC advances*, 2018, **8**, 33496–  
978 33505.
- 979 48 S. Xu, Y. Li and X. Yan, *Separation and Purification Technology*,  
980 2025, **378**, year.
- 981 49 D. R. Lide, *CRC handbook of chemistry and physics*, CRC press,  
982 2004, vol. 85.
- 983 50 P. Bouguer, *Essai d'optique sur la gradation de la lumière*,  
984 Claude Jombert, 1729.
- 985 51 Beer, *Annalen der Physik*, 1852, **162**, 78–88.
- 986 52 F. Zuo, *European journal of physics*, 2024, **45**, 065204.
- 987 53 M. Maiorov and A. Tsebers, 1979.
- 988 54 M. Maiorov and A. Cebers, *Magneto hydrodynamics*, 1983, **19**,  
989 376–380.
- 990 55 J. D. Jackson, *Classical electrodynamics*, John Wiley & Sons,  
991 2021.
- 992 56 E. W. Chuan Lim and R. Feng, *The Journal of chemical physics*,  
993 2012, **136**, year.
- 994 57 P. J. Vikesland, R. Rebodos, J. Bottero, J. Rose and A. Masion,  
995 *Environmental Science: Nano*, 2016, **3**, 567–577.
- 996 58 C. Tsouris and T. Scott, *Journal of colloid and interface science*,  
997 1995, **171**, 319–330.
- 998 59 J. Faraudo, J. S. Andreu, C. Calero and J. Camacho, *Advanced*  
999 *Functional Materials*, 2016, **26**, 3837–3858.



The data is available upon request.

